Creep deformation and failure properties of 316L stainless steel manufactured by laser powder bed fusion under multiaxial loading conditions

Richard J. Williams[a,*], Jalal Al-Lami[b], Paul A. Hooper[a], Minh-Son Pham[b], Catrin M. Davies[a]

[a]Department of Mechanical Engineering, Imperial College London. SW7 2AZ.
[b]Department of Materials, Imperial College London. SW7 2AZ, UK.

Abstract

316L stainless steel has long been used in high temperature applications. As a well-established laser powder bed fusion (LPBF) alloy, there are opportunities to utilise additive manufacturing in such applications. However, the creep behaviour of LPBF 316L under multiaxial stress conditions must first be quantified before such opportunities are realised. Uniaxial and double notched bar creep tests have been performed and characterised using power-law relations to evaluate the creep strain and rupture properties of LPBF 316L. The creep response was found to be anisotropic with specimen build orientation, with samples loaded perpendicular to the build direction (Horizontal) exhibiting 8 times faster minimum creep rates than samples built parallel to the build direction (Vertical) and significantly shorter rupture lives. This was mainly attributed to the columnar grain structure, which was aligned with the build direction of the LPBF samples. The multiaxial creep rupture controlling stress was determined and found to be a combination of the equivalent and max. principal stress. X-Ray CT measurements in selected samples illustrated that the samples were approximately 99.6% dense post-build and the quantity of damage post testing was determined. Optical and EBSD microstructural characterisation revealed intergranular creep damage present in the specimens, however rupture was ultimately trans-granular in nature and influenced by the presence and orientation of pre-existing processing defects relative to the sample build and loading direction.

Keywords: creep, selective laser melting, powder bed fusion, 316L, high temperature

*corresponding author: r.williams16@imperial.ac.uk

1 Introduction

Laser powder bed fusion (LPBF) enables the manufacture of intricate details in components, e.g. heat exchanger channels, that are difficult or impossible by conventional manufacturing techniques [1, 2]. 316L stainless steel (SS) is commonly used for the manufacture of LPBF components. When manufactured by conventional methods, 316L is widely used in applications where high temperature creep and corrosion resistance are required [3]. Recently there has been an interest in applying LPBF to manufacture 316L components for these applications [4].

It has been widely reported that 316L samples produced by laser powder bed fusion (LPBF) exhibit higher strength than those manufactured through conventional routes, and in some cases good ductility [5, 6]. However, little has been reported on the high temperature behaviour of 316L manufactured by LPBF. LPBF also generates high tensile (> 400 MPa in 316L) residual stresses [7] that are known to drive creep deformation and crack growth in high temperature applications [8, 9]. Residual stresses may be relaxed through high temperature heat treatments that activate processes including creep. Models to predict stress relaxation in LPBF components therefore require creep property characterisation.

At present the published literature on the creep behaviour of LPBF 316L is very limited. Creep resistance of small blocks manufactured by LPBF under various scanning speeds were examined using micro small punch creep test samples (10 × 10 × 0.5 mm) by Yu et. al. [10]. The samples were loaded perpendicular to the build direction and manufacturing defects were found to impact the creep resistance of the material. Interpretation of small punch test data can, however, be complicated [10] as the stress generated in the small punch sample is not uniaxial, and the thin samples will only contain around 10-20 grains through their thickness.

Most research on creep performance of LPBF material has focussed on nickel-based superalloys, given their popularity within the aerospace industry and gas turbine engines. Hautfenne et al. [11] conducted rupture tests on Inconel 718, studying the influence of different heat treatments and build orientation. Davies et al. [12] conducted a similar study on an undisclosed nickel-based superalloy. Both papers found anisotropic creep properties with respect to specimen build orientation and this was attributed to the columnar grain structure found in the LPBF microstructure. Hautfenne et al. [11] concluded that the vertical building orientation had higher creep resistance due to the columnar grain boundaries being orientated parallel to the building direction. Davies et al. [12] however concluded that the horizontally built samples had a longer creep life than the vertical samples due to a combination of the grain size and the relative absence of carbides and sigma (Σ3) type boundaries. Heat treatment and aging also led to a significant improvement in creep life, as expected in such materials. Xu et al. characterised the creep properties of IN718 and examined the impact of various post-processing operations, including hot rolling, machining and hot isostatic pressing (HIP) [13, 14]. Whilst hot rolling improved creep resistance and life significantly, machining alone was found to have a minimal impact and HIP led to worse performance despite its ability to close processing defects. Xu et al. also carried out interrupted creep tests in conjunction with X-ray computed tomography (XCT) to observe defect evolution under creep loading [15]. The initial porosity distribution was characterised, pore growth and creep void formation were described, allowing the location of failure to be predicted. However, test durations were short and thus creep mechanisms were not adequately developed at the test interruption points. Limited information was presented about defect interactions with neighbouring defects or with microstructural features.

In each work reviewed, the LPBF Nickel alloy investigated was found to exhibit shorter rupture life and higher creep strain rates than the equivalent wrought material, highlighting the need for further study in this area. Furthermore, the effects of multiaxial loading have not been considered. Components in service are often subjected to multiaxial loading conditions and the introduction of stress triaxiality typically accelerates failure. Therefore, the effect of multiaxial stresses should be considered to determine the deformation and failure behaviour of components. Finally, while there has been much focus on microstructure in the listed studies, little attention has been paid to the influence of initial processing defects on rupture. Only the paper by Xu et al. [15] has focussed on defect behaviour under creep conditions. If LPBF components containing any level of porosity are to be used in service in creep sensitive applications, understanding the impact of processing defects on failure behaviour will be essential.

In this paper, the creep deformation and rupture behaviour of LPBF 316L are studied, employing established methods for characterising creep performance. Creep rupture tests were performed on uniaxial and double notched bar specimens to assess the influence of multiaxial stress states. The effects of building orientation and initial processing defects on creep performance were also examined. The microstructure was characterised extensively, by microscopic and XCT methods, to assess the extent of creep damage and the rupture mechanism in the notched bar specimens.

The paper is structured as follows. Firstly, the background theory on creep deformation and rupture under uniaxial and multiaxial stresses is presented. The material and specimen preparation are then detailed and methods for creep rupture testing under multiaxial conditions using circumferentially notched bars are described. The results of the uniaxial and notched bar creep rupture tests are then presented, including the evaluation of the rupture controlling stress under multiaxial condition and the microstructure and porosity of the samples are analysed.

2 Creep Deformation and Rupture Behaviour

As noted above, most creep tests are performed under uniaxial loading conditions. However, components are often subjected to multiaxial loading conditions. Multiaxial stresses are known to significantly influence the creep deformation and rupture behaviour of a material. Therefore, it is important that the multiaxial creep behaviour of a material is characterised. The creep deformation and rupture life laws under uniaxial and multiaxial conditions are described below.

2.1 Uniaxial Creep Laws

For components subjected to stresses and temperatures in the power-law creep regime [16], the dependency of creep strain rate, $\dot{\varepsilon}^c$, on stress, σ, is often represented by a power-law relation

$$\dot{\varepsilon}^c = A\sigma^n \tag{1}$$

where n is the power-law creep stress exponent and A is a temperature dependent material constant.

The power-law expression of Eqn (1) is widely used to describe the creep strain rate during secondary creep and is commonly referred to as the Norton creep law [17]. The constants A and n are therefore obtained by fitting to the secondary region observed in uniaxial creep test data. Note that the applied stress, σ, in a uniaxial creep test may be considered an equivalent stress, and hence Eqn (1) can be used under both uniaxial and multiaxial creep conditions.

Similarly, the time to rupture, t_r, in a uniaxial creep test over a given stress range can often be approximated by a power-law relation,

$$t_r = B_r \sigma^{-v_r} \tag{2}$$

where B_r and v_r are a temperature dependent constant that are obtained by fitting to uniaxial creep test data.

2.2 Multiaxial Creep Rupture Law

It has been observed from the analysis of multiaxial stress creep rupture tests, usually in the form of notched bar creep tests [18], that the creep rupture time in certain materials is governed by the maximum principal stress, σ_1, or the equivalent stress, σ_{eq}, or a combination of both stresses [19]. This stress combination is here referred to as the rupture controlling stress, σ_{RC}.

Several formulations of σ_{RC} based on the equivalent stress and maximum principal stress have been proposed. One of the most popular is that proposed by Leckie and Hayhurst [19, 20] and this is also one of the preferred forms listed in the code of practice for conducting notched bar creep rupture tests [18]. This formulation of the rupture controlling stress was chosen for the present analysis, given by:

$$\sigma_{RC} = \alpha_{RC}\sigma_1 + \left(1 - \alpha_{RC}\right)\sigma_{eq} \tag{3}$$

where α_{RC} is material parameter determined from sets of creep tests on notched specimens, carried out under different multiaxial stress states ($0 \leq \alpha_{RC} \leq 1$). The value of α_{RC} can also be indicative of the failure process. A value $\alpha_{RC} = 0$ indicates that failure is controlled the equivalent stress, and is hence deformation controlled, whereas if $\alpha_{RC} = 1$ failure is fully controlled by the maximum principal stress and hence is considered to governed by intergranular void growth [18]. Generally, for austenitic stainless steels $0 < \alpha_{RC} < 1$ [21, 22], thus failure is controlled by a combination of deformation and void growth.

3 Specimen Manufacture and Testing Methods

3.1 Material and specimen preparation

316L round bars of dimensions 14 mm × 100 mm were manufactured using a Renishaw AM250. A ‘chessboard’ hatching strategy was used with 67° rotation of the hatching angle between layers. The processing parameters are listed in Table 1. To assess the influence of building orientation on creep properties, the bars were manufactured in two orientations here denoted vertical (V) (parallel to build direction) and horizontal (H) (perpendicular to the build direction). The chemical composition of the powder used to manufacture the bars is given in Table 2.

Table 1: Processing parameters used to manufacture the LPBF 316L bar.

Parameter	Value	Unit
Laser power	200	W
Point distance	60	µm
Exposure time	80	µs
Hatch spacing	110	µm
Spot size	65	µm
Layer thickness	50	µm

Table 2: Nominal chemical composition of the 316L powder used to manufacture the specimens.

C	Cr	Cu	Fe	Mn	Mo	N	Ni	O	P	S	Si
0.030	17.0-18.0	0.75	Balance	2.00	2.00-2.50	0.10	12.00	0.10	0.030	0.015	0.75

Uniaxial and double notched bar specimens of the same overall dimensions were then machined from the bars, i.e. vertical specimens were machined from the vertically built bars and horizontal specimens were machined from the horizontally built bars. The double notched bar specimens were manufactured with two different notch designs which, as per the standard [18], are denoted 'medium' and 'large'. They can be characterised in terms of their notch acuity, or sharpness, and possess notch throat diameter (d_{no}) to notch radius (R_{no}) ratios of 10 and 3, respectively. An engineering drawing of the double circumferentially notched bar specimen is shown in Figure 1, with the details and dimensions of the notches inset. The uniaxial test specimens were of the same general dimensions but excluded the notches.

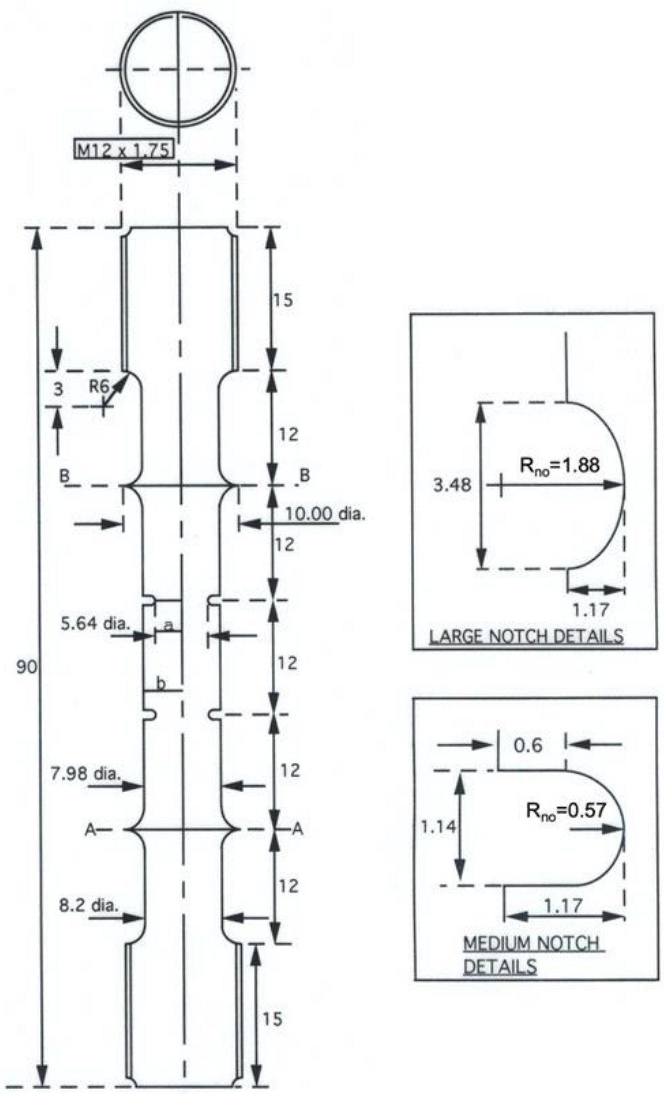

Figure 1: Engineering drawing of the double circumferentially notched bar test specimen. Details of the two different notch designs are inset. In both cases, the notch throat diameter d_{no} = 5.64 mm, giving $\frac{d_{no}}{R_{no}}$ of 3 for the medium notch and 10 for the large notch. All dimensions are in mm.

3.2 Creep test procedure

Constant load uniaxial and notched bar creep rupture tests were performed at 650 °C using dead-weight loaded creep rigs. To determine the stress dependency of uniaxial creep strain rates and rupture times, a range of loads were applied to the specimens to achieve reasonable failure times that were long enough to allow creep processes to develop, whilst causing rupture in a practical time frame. This dictated that the vertical and horizontal built specimens were tested at different stress levels.

K-type thermocouples were attached to the gauge of the sample and the temperature was logged across all tests to ensure it did not deviate more than ±2 °C from the set point. Axial strain across the sample gauge length was monitored using two linear variable displacement transducers (LVDT), located outside of the furnace and attached across the sample gauge via extensometry. These displacements were used to calculate the secondary creep strain rate in the uniaxial tests.

3.3 Notch Bar Test Analysis

3.3.1 Failure Strain Estimate

In notched specimens the strain is highly localised around the notch throat so a global measurement of gauge extension will not characterise deformation accurately in the notch region. A local estimate of the failure strain can be estimated from a measure of the true hoop strain at the external diameter of the notch throat [23],

$$\varepsilon_\theta = \ln\left(\frac{d}{d_i}\right) \tag{4}$$

where d_i is the initial diameter of the notch throat and d is the notch throat diameter at a given instance in time. At failure, $d = d_f$, the final diameter of notch throat.

3.3.2 The Skeletal Stress Approach

Skeletal point stress techniques have been widely used to analyse creep in notched bar geometries [24-26]. In general, the exact distributions of equivalent and maximum principal stress, and therefore degree of triaxiality, across the notch throat are dependent upon the power-law creep exponent, n. However, it has previously been shown that a position exists near the notch root where the stress state in the specimen is approximately independent of the creep exponent n, notch acuity and time [18, 27]. This location is referred to as the 'skeletal point'. The location of the skeletal point is a function solely of the notch acuity and is in approximately the same position regardless of whether the equivalent, maximum principal or mean stress are considered. The location of the skeletal point for the two notch designs used in this work were taken from the results of finite element analyses reported in literature [27].

Comparison of the stress state at the skeletal point in test specimens is a method which has widely been used for characterising the multiaxial creep behaviour of notched bars [21, 28, 29] and a code of practice has been established [18]. Conditions at the skeletal point are assumed to be appropriate to characterise the overall rupture behaviour of notched bars under multi-axial conditions [18].

Ratios of the equivalent stress at the skeletal point, $\sigma_{eq,sk}$, and maximum principal stress at the skeletal point, $\sigma_{eq,sk}$, to the net section stress at the notch throat, σ_{net}, were determined previously through finite element studies [27] and are shown in Table

3. These ratios are a function of the notch acuity and were determined for a range of notch designs. This enables the stress state at the skeletal point to be calculated knowing only net section stress at the notch throat. In this work, the skeletal stress ratios in Table 3 were used to calculate the equivalent and principal stress at the skeletal point in the double notched bar specimens in accordance with the code of practice [18].

Once α_{RC} is known, σ_{RC} can then be plotted against the time to rupture and data for various notch acuities, including uniaxial conditions, should fall on the same trendline. The rupture controlling stress evaluated at the skeletal point can then be used with Eqn (2) to estimate multiaxial rupture lifetime based on uniaxial rupture data.

Table 3: Normalised skeletal stress ratios for the two different notch acuities.

Notch	$\frac{d_{no}}{R_{no}}$	$\frac{\sigma_{eq,sk}}{\sigma_{net}}$	$\frac{\sigma_{1,sk}}{\sigma_{net}}$
Large	3	0.77	1.05
Medium	10	0.66	1.14

3.4 Microstructure Characterisation

The stress is highly concentrated at the notch throat due to the reduction in cross-sectional area. Therefore, creep damage is accelerated at the two notches compared to the rest of the specimen. After testing, the intact notches of the notched specimens were sectioned, mounted and polished for inspection. The polished surfaces were electro-etched in a solution of 10% oxalic acid for approximately 20 seconds, with a voltage of 2.5 V applied to the specimen. Observation of the microstructure provided information about the formation of creep cavities in the notched gauge regions (in particular at grain and melt pool boundaries) and thus the level of creep damage accumulated at the notch.

Characterisation of the polished and etched surfaces was made by optical microscopy (OM), scanning electron microscopy (SEM) and electron backscatter diffraction (EBSD). The OM images were acquired on an Olympus microscope and SEM images were scanned on the Zeiss Auriga FEG-SEM in secondary electron (SE) mode. The EBSD scans were again made with the Zeiss Sigma 300 FEG-SEM at an accelerating voltage of 20 kV. Step sizes between 0.3 − 0.5 μm were used in the scans. The exact step size used to produce each image is noted in the figure caption. A grain boundary definition of 5° misorientation and a kernel size of 3 × 3 pixels were used in post-processing.

3.5 Volumetric Defect and Damage Quantification

To observe build processing defects and the development of creep damage volumetrically in the specimens, X-ray computed tomography (XCT) scans were performed using a Nikon Metrology HMX ST 225. Scans were made in the notched region of one vertical specimen which had undergone significant creep, circa 2000 hours, to characterise the damage state in the notched region. The initial build defect distribution present in the specimens can be represented by the region above and below the notch, as little creep deformation is known to occur in these regions of the notched bar [30]. The XCT scanning parameters used in each scan are summarised in Table 4. The raw data output from the scanner was converted to 8 bits TIFF format using ImageJ software [31]. An isotropic voxel size of 6.7 μm was achieved in the notches of the specimen and a size of 8 μm in the threads. In addition, a minimum of 5 pixels was defined to constitute a pore. This resulted in a minimum detectable defect size of around 15 μm in normalised length (i.e. the cube root of the volume).

Table 4: Parameters used in each XCT scan.

Parameter	Notch	Threads	Unit
Filter	1.5 mm copper	1.0 mm tin	-
Voltage	160	200	kV
Current	44	50	µA
Exposure	1000	1000	ms
Voxel size	8.0	6.7	µm

The resulting image stack was thresholded and binarised in Python, using the OpenCV library [32] to segment the data and identify the regions of porosity and solid material. 3D reconstruction of the segmented images was scripted in Python, using the PyVista library for data visualisation [33]. The segmented defect image stack was analysed to characterise the defect distribution in the notch and the threads, using the OpenCV and Skimage [34] libraries. Identified defects were labelled and numbered and the following parameters were extracted: centroid coordinates of the defect, defect volume, and the major and minor axis of the equivalent ellipsoid of the defect. The overall density of each scanned region was also calculated.

4 Creep Deformation and Rupture Results

4.1 Uniaxial Test Results

The creep strain development with time for the uniaxial creep tests is shown in Figures 2(a) and (b) for the vertical and horizontal specimens, respectively. Little primary creep is seen across all tests in Figure 2. Most of the test duration, up to 80 % of the rupture time for the vertical samples and 50% for the horizontal samples, is in the secondary creep regime. The lack of primary creep may be attributed in part to the high initial dislocation density of LPBF material [35], meaning there is little ability for the material to harden further.

The rupture time is plotted against the applied stress for both vertical and horizontal uniaxial test specimens in Figure 3 (a). Significant scatter is seen in the data, however a power-law fit (Eqn 2) has been made to both data sets. The corresponding rupture constants, B_r and v_r, are given in Table 5. For the stress range examined, the stress to cause failure in a given time is approximately 30% higher for the vertical samples compared to the horizontal samples.

For the stresses and temperatures considered, both the horizontal and vertical specimens are expected to be dominated by power-law creep mechanisms. The secondary creep strain rate is plotted against the applied stress in Figure 3(b) and a power-law fit (Eqn 1) made to the vertical and horizontal samples shown. The corresponding power-law creep constants, A and n, are given in Table 6. The creep strain at failure (creep ductility) and time to rupture of the uniaxial test samples are detailed in Table 7. Since the creep strain rate data available for the horizontal samples was limited, the power-law parameters could not be determined accurately. The creep stress exponent n for the horizontal samples was therefore assumed the same as the vertical samples as there is greater confidence in the value determined for vertical specimens. This value (5.7) is typical of power-law creep [16]. The constant A (Eqn (1)) was then determined to provide a best fit to the horizontal data when n = 5.7. As can be seen in Figure 4(b), and Table 6, for a given stress, the creep strain rate for the horizontal samples is around a factor of 8 higher when compared to the vertical samples.

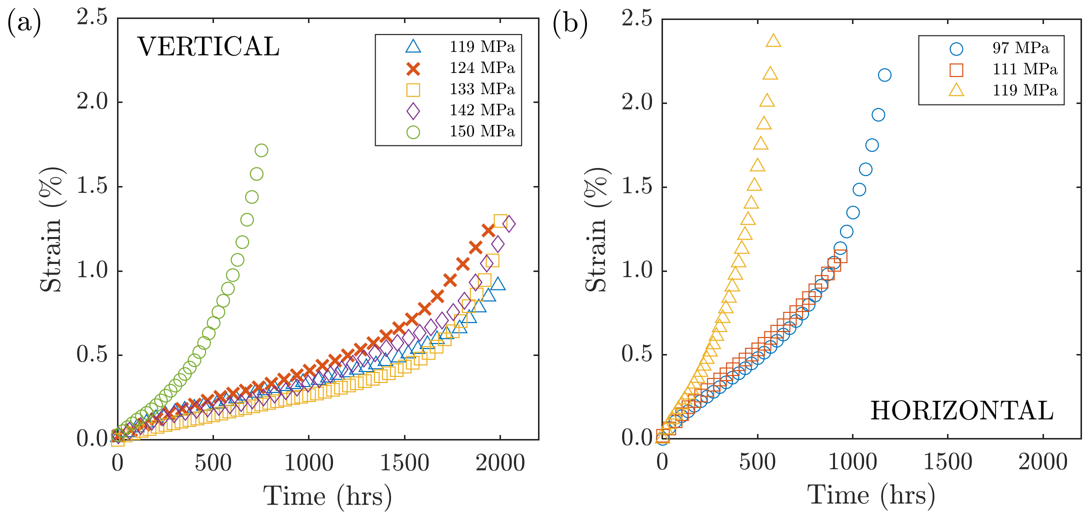

Figure 2: Uniaxial creep curves for the (a) vertical and (b) horizontal samples.

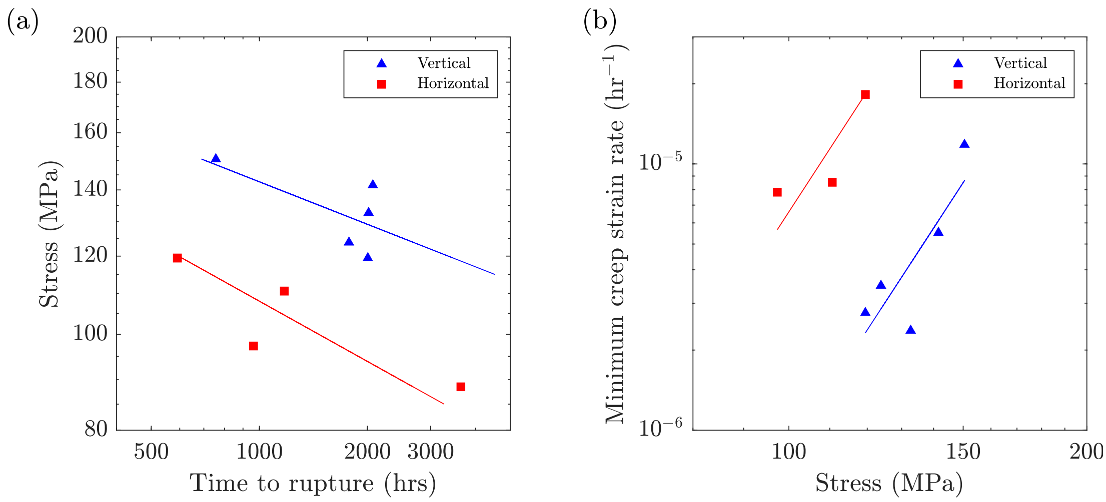

Figure 3: (a) Creep rupture and (b) creep strain rate against stress for the horizonal and vertical uniaxial test specimens

Table 5: Creep rupture constants for the two different specimen orientations (note the constants are determined for stress in MPa and time in hours).

Build orientation	B_r	v_r
Vertical	1.1×10^{18}	7.0
Horizontal	1.1×10^{13}	4.9

Table 6: Power-law creep constants for the two different specimen orientations (note the constants are determined for stress in MPa and time in hours).

Build orientation	A	n
Vertical	3.0×10^{-18}	5.7
Horizontal	2.5×10^{-17}	5.7

Table 7: Rupture life, minimum creep strain rate and creep ductility of the uniaxial test specimens.

Build orientation	Stress (MPa)	Time to rupture (hrs)	Min. creep strain rate (hr^{-1})	Strain at failure (%)
Vertical (V)	119	2004	2.8×10^{-6}	1.4
	124	1776	3.5×10^{-6}	1.7
	133	2016	2.4×10^{-6}	1.5
	142	2070	5.5×10^{-6}	1.6
	150	757	1.2×10^{-5}	1.9
Horizontal (H)	88	3640	–	-
	97	963	7.8×10^{-6}	1.0
	111	1173	8.5×10^{-6}	2.3
	119	591	1.8×10^{-5}	2.5

It can be seen in Table 7 that the axial strain at failure, measured along the samples gauge length, is relatively low for all tests compared to conventionally manufactured material, being on average 1.6% and 1.9% for the vertical and horizontal samples, respectively, and at maximum 2.5%. This low creep ductility may indicate a strong influence from build defects. Build defects are well known to adversely affect the ductility of LBPF specimens under regular, quasi-static conditions

4.2 As-built microstructure

The grain morphology of the two build orientations can be seen in EBSD maps taken from vertical and horizonal manufactured specimens in Figure 4. The maps were made on a cross-sectional plane parallel to the building direction and hence display the grain structure along the build direction. LPBF material is known to exhibit a columnar grain structure, where the columnar growth direction is aligned with the building direction [36]. The scans were made on specimens in the as-built condition, prior to creep testing.

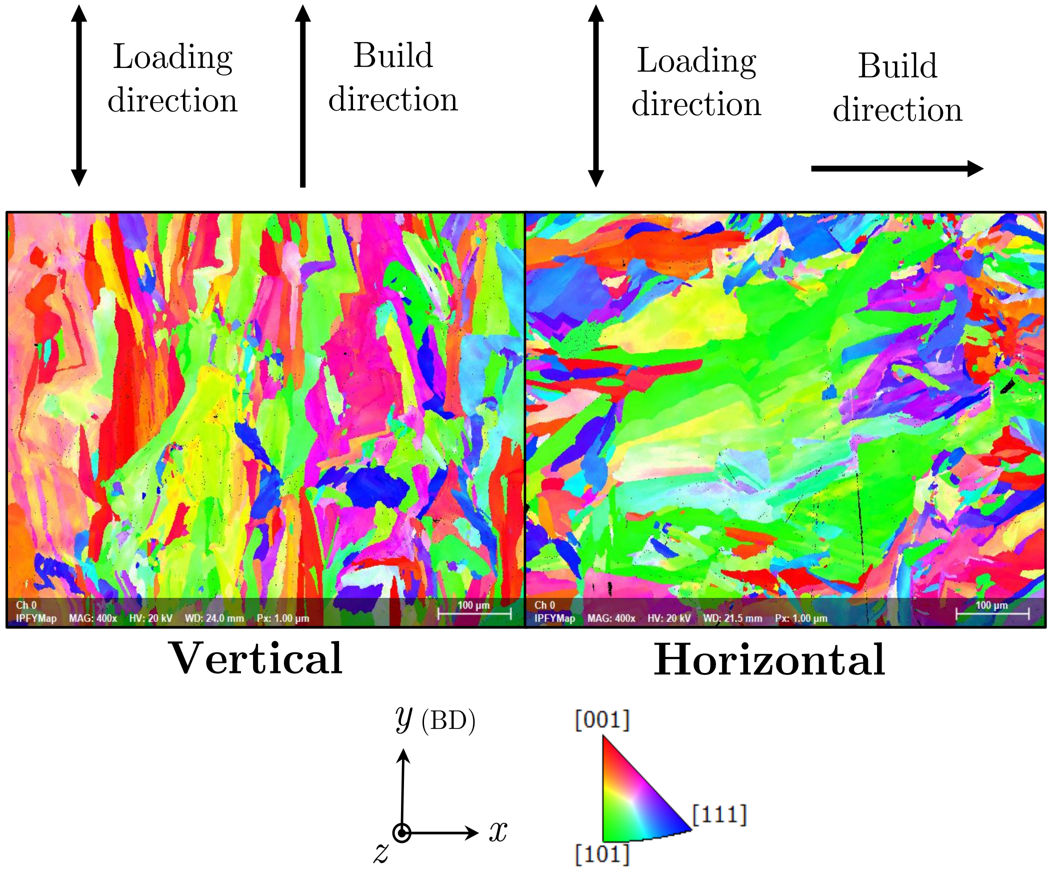

Figure 4: EBSD IPF-*y* maps of a cross-section parallel to the loading direction in a vertical specimen and a horizontal specimen, in the as-build condition and prior to testing.

A columnar grain structure is evident in Figure 4, with grains extended in the build direction and shorter in the orthogonal direction. The EBSD maps are oriented relative to the loading direction. This highlights that the grain size is much larger along the loading direction in the vertical specimens than in the horizontal specimens, owing to the columnar grain structure. Accordingly, there is a lower area of grain boundaries perpendicular to the direction of loading in the vertical specimen compared with the horizontal specimen.

4.3 Notched Bar Test Results

4.3.1 Notched Bar Creep Rupture Data

A summary of the notched bar test results are given in Table 8, where the hoop strain of the unfailed notch (Eqn (4)) at specimen failure is reported. Generally, the higher the notch acuity, the lower the strain at failure, as expected. This is due to the increase in stress triaxiality, and hence creep deformation rate, and increases the mean and maximum principal stress, thus promoting creep void growth and hence failure. However, of the horizontal samples, test HB4 shows a very low strain at failure, which may indicate the influence of build defects.

Table 8: Sample details, rupture times and final hoop strain in un-failed notched in double notched bar tests.

Specimen code	Build orientation	Notch acuity	Net Stress (MPa)	$\sigma_{eq,sk}$ (MPa)	$\sigma_{1,sk}$ (MPa)	Time to rupture (hrs)	ε_θ (%)
VL1	V	3	141	109	149	1593	1.18
VL2	V	3	150	116	158	876	0.55
VL3	V	3	159	123	167	1136	0.92
VL4	V	3	194	150	204	93	0.53
VM1	V	10	150	99	171	1210	0.35
VM2	V	10	159	105	181	3365	0.69
VM3	V	10	168	111	191	917	0.25
VM4	V	10	177	117	202	364	0.28
HL1	H	3	124	95	130	1547	0.62
HL2	H	3	129	99	136	867	0.66
HL3	H	3	133	102	139	1200	N/A[1]
HL4	H	3	159	123	167	620	0.09
HM1	H	10	115	76	131	1872	0.53
HM2	H	10	124	82	141	754	0.44
HM3	H	10	133	88	151	1884	0.46
HM4	H	10	141	93	161	521	0.35

The net section stress (the applied load divided by the initial cross-sectional area at the notch throat) is plotted against the time to rupture for the notched bar and uniaxial specimens in Figure 5, for the (a) vertical, and (b) horizontal samples. This enables the notch strengthening factor to be determined. The notch strengthening factor is defined as the ratio of net section stresses in notched and uniaxial specimens that produce the same rupture life. A value greater than 1 indicates notch strengthening behaviour. Figure 5 shows a higher net section stress in notched specimens than uniaxial, for a given time to rupture, in almost all tests. Therefore, LPBF 316L demonstrates notch strengthening behaviour. This is in line with previous findings on wrought CM 316 series steel [22] and may be expected for a generally ductile steel such as 316L [37].

Figure 6 shows the rupture controlling stress against the time to rupture for the uniaxial and notched bar specimens. The dashed lines indicate ± 2 standard deviations in the mean fit to the uniaxial data, which represents the scatter in the data. The rupture controlling stress was calculated from the stresses at the skeletal point using Eqn (3) and the parameter α_{RC} in Eqn (3) was estimated to be 0.45 for the vertical specimens and 0.30 in the horizontal built specimens. These values, which are comparable to those found in previous work on wrought austenitic stainless steel [21, 22] , imply that for the stress range considered, creep rupture is controlled by a combination of the equivalent and maximum principal stresses, with creep deformation dominating failure [18]. In Figure 6, all the notched bar data falls within two standard deviations of the indicating the suitability of the values of α_{RC} estimated and that the degree of scatter in the notch bar data is similar to the uniaxial data.

[1] Strain at failure could not be determined

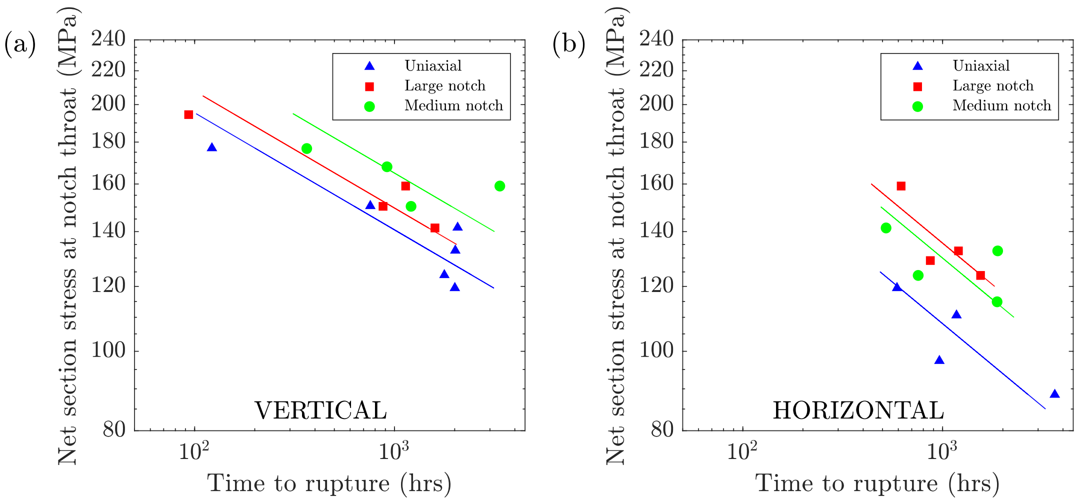

Figure 5: Plots comparing the net section stress against time to rupture for the (a) vertical, and (b) horizontal uniaxial and notched specimens. Both building orientations exhibit notch strengthening behaviour.

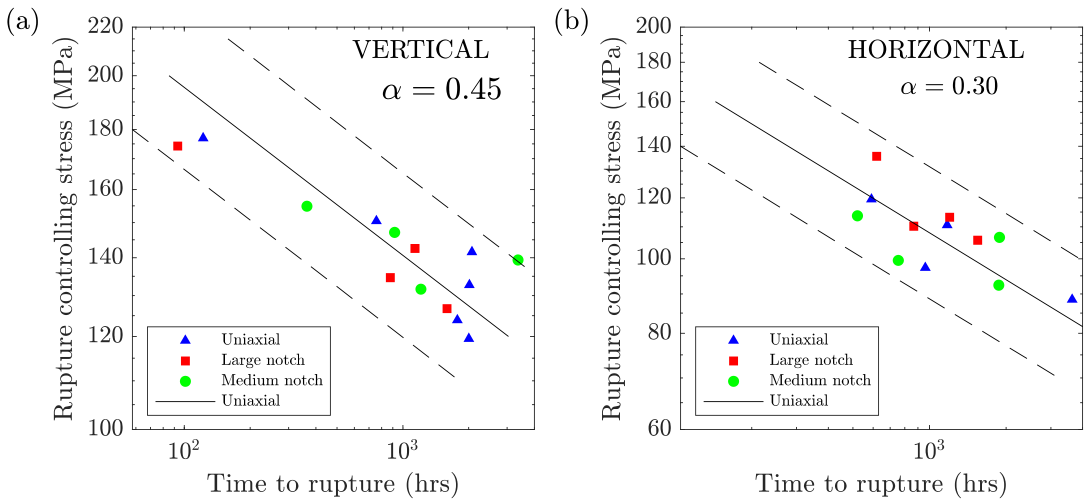

Figure 6: Plot of the rupture controlling stress against time to rupture for the (a) vertical, and (b) horizontal specimens. The rupture stress was calculated according to Equation 4 using the alpha values indicated. The dashed black lines indicate 2 standard deviations of the power-law fit of the uniaxial data.

5 Build Defect and Creep Damage Analysis

5.1 X-ray Computed Tomography Results

The volumetric reconstruction of the XCT scans on both halves of the intact (un-fractured) notch region of sample VM2 (see Table 8) are shown in Figure 7. The volume was segmented to isolate defects and these are rendered in red against a blue semi-transparent mask of the solid part. The percentage values annotated on the figures quantify the overall defect volume fraction in the corresponding region of the sample.

As shown in Figure 7, the defect volume fraction away from the notch root, was around 0.3 - 0.4% which indicates the quantity of defects resulting mainly from the build process. These values are similar to the defect volume fraction were measured in the threaded ends which are not influenced by creep strain (0.28% in the top thread and 0.39% in the bottom thread). These defects appear to be consistent in character with typical lack of fusion defects, though the defects range in size and morphology. Despite the appearance of notable build defects, the overall volumetric density of the as-built material was greater than 99.5% which is often considered acceptable [38].

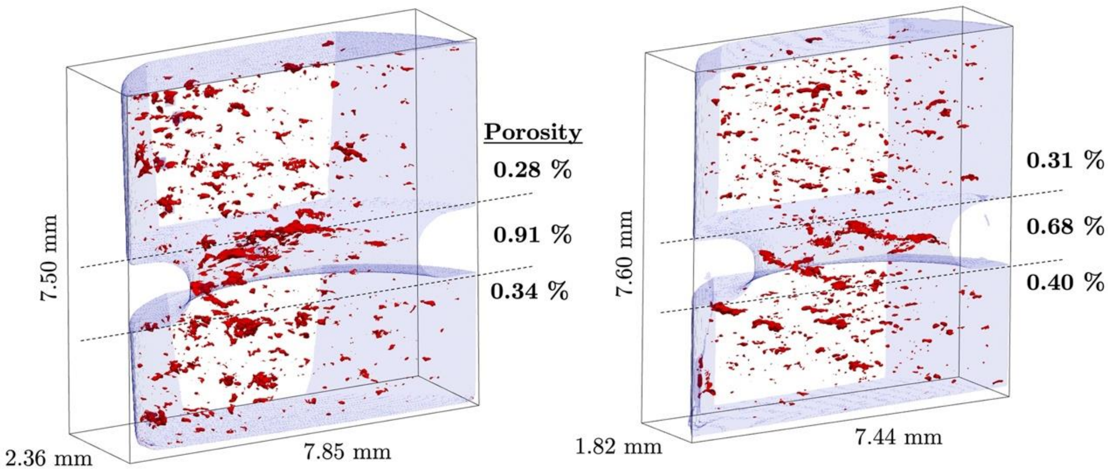

Figure 7: Reconstructed XCT scan of the intact notch of the specimen VM2 in two halves following sectioning.

The defect concentration and characteristics did not appear to change significantly between the threads and the un-notched gauge section of the specimen. Larger micro-cracks can be seen in the notch region, which appear to be branching and linking through several build defects and across multiple build layers (note the specimen shown in Figure 7 was built in the vertical orientation and hence build layers are parallel to the expected crack growth direction). This contributes to the higher overall defect volume fraction of around 0.7 - 0.9% measured in the notch region.

Creep cavities could not be detected by XCT as they are much smaller than 10 µm in size, thus only creep damage in the form of micro-cracks, resulting from creep void growth and coalescence, could be resolved. Microscopic observations using scanning electron microscope (SEM) were performed to study the formation of creep cavities and smaller micro-cracks.

5.2 Microscopic observation of crept conditions

The results of the microstructural characterisation of the notch region of selected vertical medium notched samples are presented here. An SEM micrograph is shown in Figure 8 from sample VM2 and an EBSD scan is shown in Figure 9 from sample VM1. Creep micro-cracks can be seen growing perpendicular to the loading direction from existing build defects. These cracks can coalesce and link build defects located on different build layers, confirming the observations made in the XCT scan (Figure 7).

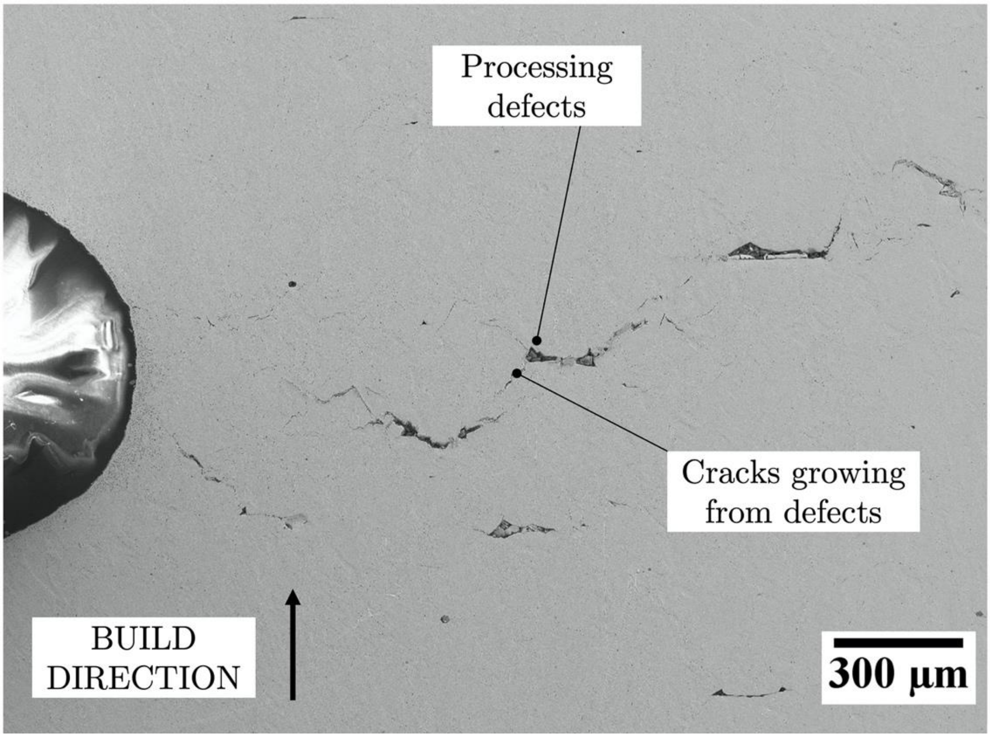

Figure 8: SEM image of creep damage ahead of the notch tip in vertical sample VM2.

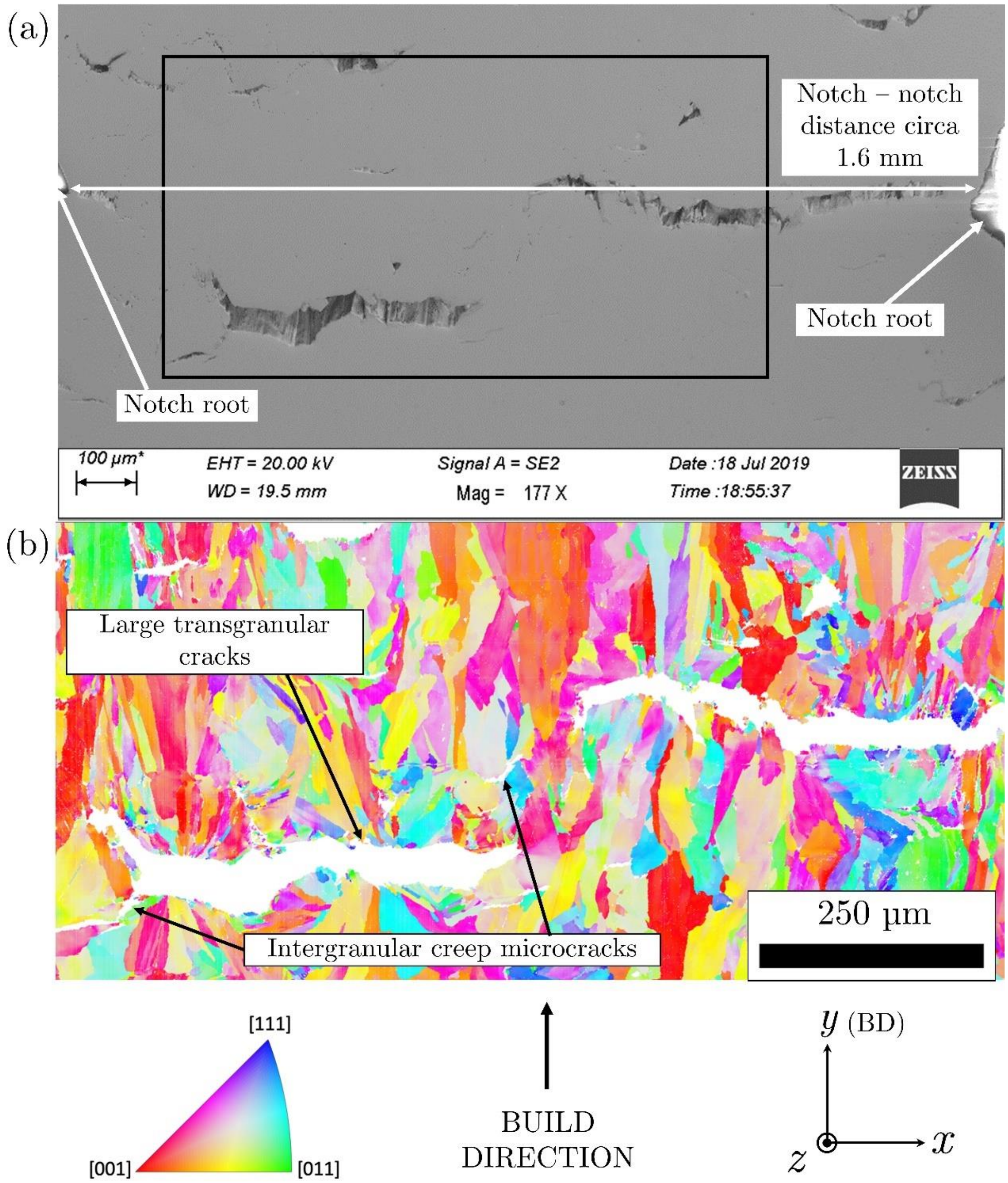

Figure 9: (a) SEM image of creep cracks in the notch region of specimen VM1; (b) EBSD IPF-*y* map in the same location as (a). The map was produced with a 0.5 µm pixel size.

Figure 9 shows an EBSD map of the unfailed notch in sample VM1. This notch was clearly at the onset of failure as large trans-granular cracks can be observed across the sample which appear to have extended from lack of fusion porosity. Such trans-granular cracks will have resulted from the increase in stress due to notch diameter reduction and stress concentration from nearby creep damage and lack of fusion porosity. Some intergranular creep microcracks can also be observed (to the left of the image) which appear to have initiated from the lack of fusion pore which acts as an additional stress concentration feature.

Sites of intergranular and trans-granular damage in the notched specimen VM2 are observed in the optical microscopy (OM) and scanning electron microscopy (SEM) images shown in Figure 10 and the EBSD map shown in Figure 11. The OM image in

Figure 10 (b), which is an enlarged view of Figure 10 (a), shows significant intergranular creep cavitation and several instances where creep cavities have coalesced to form intergranular micro cracks. Larger cracks can also be seen but it is unclear whether they are trans-granular or intergranular in nature. Figure 10(b) also shows small spherical gas pores present, however these do not appear to have been affected by creep deformation and thus are not considered to be influential in the failure process of the samples, in contrast to the lack of fusion type porosity. Creep cracks are clearly visible ahead of the notch tip in the SEM image shown in Figure 10(c).

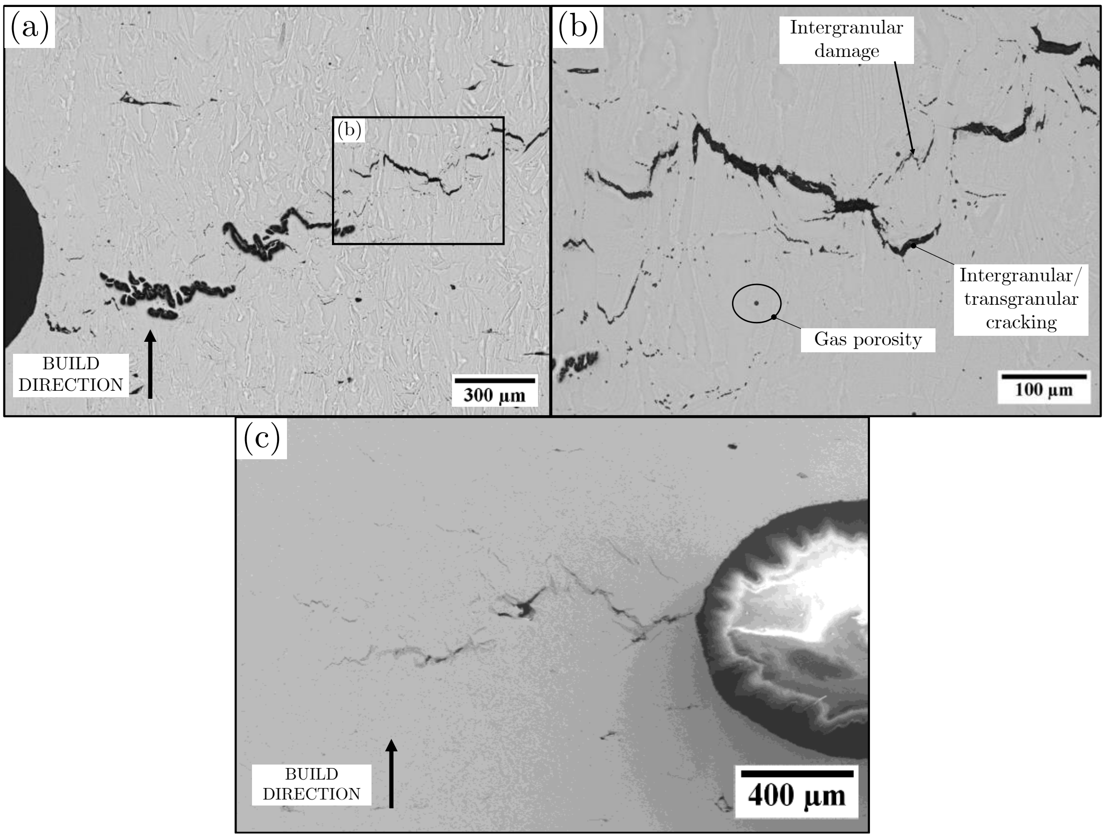

Figure 10: Micrographs displaying sites of creep damage in the notch region of specimen VM2, acquired by OM (a, b) and SEM (c). (b) is a zoomed view of the region of interest in (a). (c) was acquired at a voltage of 20 kV in secondary electron (SE) mode.

The EBSD grain map shown in Figure 11 confirms the presence of significant intergranular cracks, that result from the creep damage process at grain boundaries. Larger cracks can be seen to the left of the image which appear to be intergranular. The discontinuous nature of creep damage development, which depends on factors such as crystallographic texture and grain boundary orientation, can lead to the development of highly stressed uncracked ligaments, which may eventually fail by plasticity and hence may be trans-granular in nature. Such cracks appear similar to the larger cracks seen to the left hand side in Figure 10 (a) and (b). However, the cracks are significantly narrower than those growing from the processing defects as shown in Figures 8 and 9.

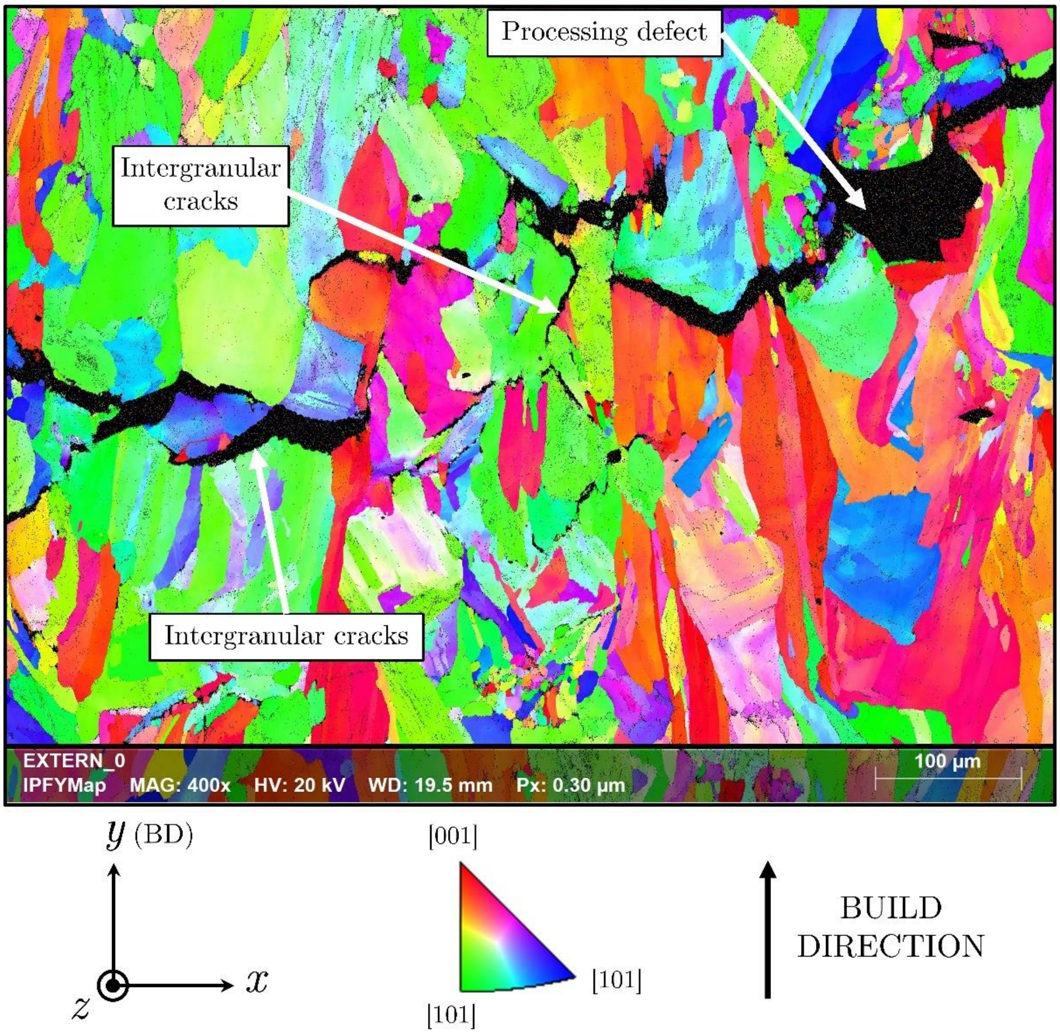

Figure 11: EBSD IPF-*y* map of creep damage in the notch region of specimen VM2. The EBSD map was acquired at ×400 magnification, with a step size of 30 µm.

6 Discussion

Though the number of tests performed in this work is limited, and significant scatter has been seen, some clear trends have been observed. The grain morphology and initial processing defects have significantly influenced the creep deformation and failure behaviour of LPBF samples.

Creep mechanisms, both dislocation and diffusion creep, rely on the diffusion of atoms. Diffusion is accelerated by the presence of atomic vacancies, hence grain boundaries and dislocation cores form high diffusivity paths. The creep rate strongly depends on grain size, as smaller grains result in larger grain boundary areas. Diffusion is also dominant in the max. principal stress direction as the atomic spacing and vacancies are increased.

Columnar grains were found to grow in the build direction. For horizontally built samples, the loading and hence principal stress direction was perpendicular to the build direction and the majority of the grain boundary area. In this case, the grain size was relatively small along the direction of loading and therefore the diffusivity path is relatively short. In addition, grain boundary diffusion is assisted by the max principal stress.

In contrast, the vertically built specimens were loaded parallel to the direction of columnar grain growth and therefore the max principal stress was mostly parallel to the grain boundaries. In this case the grain size is relatively large along the direction of loading, compared to the horizontal case, and diffusion paths are longer. Thus, horizontal specimens exhibited higher creep strain rates and shorter failure times compared to vertical specimens.

However, as noted in Table 6, marginally higher failure strains (creep ductility) were found in the horizontal samples. In the notch bar tests, creep damage development, and thus the ultimate failure process, was found to initiate and grow not only from the notch root but significantly from existing build defects in particular lack-of-fusion pores that usually have irregular morphologies. Therefore, existing build defects are fundamental to the failure process. These defects act as local stress concentration features that could induce high stress triaxiality and local plasticity, depending on their shape and location in the sample. This may be particularly deleterious for the vertical samples, which are loaded perpendicular to the build planes, as build defects tend to be relatively planar in shape, and located along the build plane (as seen in Figure 7). The effect of build defects on plastic ductility has been described and explained in [38], where defects were found to significantly reduce the plastic ductility, especially in vertically built tensile samples. As illustrated in [38], these build defects therefore have high a stress concentration ratio and induce significant damage, across a given cross-section normal to the build direction. Hence, build defects are expected to reduce the creep ductility of vertical samples compared to horizontal samples in the similar way as the uniaxial plastic tensile ductility in [38].

For notch bar samples, stresses ahead of the notch tip are triaxial. Thus, even if the grains are elongated in the applied load direction (as in the vertical samples), since the volume of material ahead of the notch is stressed in 3 orthogonal directions, the influence of grain morphology on the creep deformation rate may be less for the notched bars than the uniaxial bars. Noting the value of α_{RC} determined in the rupture controlling stress (Eqn (3)) for this material, failure is generally influenced more by the equivalent stress than the maximum principal stress. However, the grain boundary area and build defect orientation relative to the maximum principal stress remains important for creep damage development and thus failure. Therefore, as can be seen in Figure 5 and Table 8, the net stress to cause rupture in a given time was generally around 30% lower for the horizontal notched bars than the vertical, following the trend observed in the uniaxial specimens.

Though notch acuity generally had the expected effect on creep rupture, significant scatter exists in the results. This scatter may be attributed to the influence of build defects. Since, as explained above, these defects acted as additional stress concentrations that creep microcracks nucleated at and grew from. The damage, regardless of the mechanism, appeared to be distributed fairly evenly across the notch throat. Insignificant damage was observed in regions above and below the notch, highlighting the influence of the stress triaxiality on damage. Although intergranular cracks and cavity nucleation were found extensively in certain locations in the notch region of the samples, ultimate sample failure was found to be a result of trans-granular, plasticity-induced rupture of highly stressed uncracked ligaments between micro-cracks or due to several build defects located in close proximity in the notch region coalescing through trans-granular creep crack growth.

For each individual specimen, the size, shape and location of build defects can significantly impact failure. Specimens with several large defects located close together in the notch region and near the outer surface are likely to suffer more rapid failure than with when spread further apart. Hence, in the results shown here, only a weak correlation was seen between applied stress and rupture life.

The quantity of residual stress in these samples are considered negligible since, as shown in [39], the majority of stresses would have relaxed during the sample machining process. However, components in the as-built (i.e. not machined) condition will have high tensile stresses near their surfaces, where build defects may also exist. These residual stresses will relax rapidly with time at temperatures in the creep regime [7], with accompanying deformation.

The results of this work imply that build defects are detrimental to the creep life of 316L components manufactured by LPBF. Lifetime assessment procedures for conventionally welded high temperature components typically rely on the assumption that a postulated defect exists in the welds that may not have been detected by non-destructive evaluation techniques [40]. Thus, the design and lifetime assessment of LPBF components should also consider the impact of probable build defect size, shape and volume fraction, in addition to the global stress state of the component.

7 Conclusions

The creep deformation and rupture behaviour of LPBF 316L under uniaxial and multiaxial stress conditions at 650 °C have been characterised using uniaxial and notch bar samples built in the horizontal and the vertical direction. For a given stress, the secondary creep strain rates of the horizontally built samples were found to be around a factor of 8 higher than the vertical samples, and the horizontal samples generally had shorter failure times. The anisotropy was attributed to the vertically (build direction) columnar grain structure of the LPBF material, which result in the grain boundaries being normal to the max principal stress in the horizontal samples, thus promoting grain boundary diffusion. The skeletal stress approach was employed to characterise multiaxial creep rupture controlling stress, which was found to be a combination of the equivalent stress and max principal stress (α_{RC} = 0.45 and 0.30 were determined for vertical and horizontal specimens, respectively). X-ray computed tomography and microscopy revealed that build defects strongly influenced the creep damage development and rupture behaviour. Creep damage in the form of intergranular voids and micro-cracks were found to develop from these build defects. For closely neighbouring defects, creep microcracks could extend between them, and trans-granular cracks were developed in highly stresses ligaments between build defects and creep cracks, ultimately leading to final rupture. The results of this study can inform stress relaxation heat treatment simulations and continuum creep damage models.

Acknowledgements

The authors thank AWE plc (contract 30338995) for funding Richard Williams for his PhD studies and Paul Hooper’s research fellowship.

8 References

1. Wong, M., et al., *Selective laser melting of heat transfer devices.* Rapid Prototyping Journal, 2007. **13**(5): p. 291-297.
2. Jafari, D. and W.W. Wits, *The utilization of selective laser melting technology on heat transfer devices for thermal energy conversion applications: A review.* Renewable and Sustainable Energy Reviews, 2018. **91**: p. 420-442.
3. Kosmac, A., *Stainless Steels at High Temperatures*, in *Materials and Applications Series*. 2012, Euro Inox: Brussels.
4. Beard, W., et al., *Fatigue Performance of Additively Manufactured Stainless Steel 316L for Nuclear Applications*, in *Proceedings of the 30th Annual International Solid Freeform Fabrication Symposium*. 2019.
5. Wang, Y.M., et al., *Additively manufactured hierarchical stainless steels with high strength and ductility.* Nature Materials, 2017. **17**: p. 63-71.
6. Pham, M.S., B. Dovgyy, and P.A. Hooper, *Twinning induced plasticity in austenitic stainless steel 316L made by additive manufacturing.* Materials Science and Engineering: A, 2017. **704**: p. 102-111.

7. Williams, R.J., et al., *Effects of heat treatment on residual stresses in the laser powder bed fusion of 316L stainless steel: finite element predictions and neutron diffraction measurements.* Journal of Manufacturing Processes (in press), 2020.
8. Turski, M., et al., *Residual stress driven creep cracking in AISI Type 316 stainless steel.* Acta Materialia, 2008. **56**(14): p. 3598-3612.
9. Skelton, R.P., et al., *Factors affecting reheat cracking in the HAZ of austenitic steel weldments.* International Journal of Pressure Vessels and Piping, 2003. **80**(7): p. 441-451.
10. Yu, J.M., V.H. Dao, and K.B. Yoon, *Effects of scanning speed on creep behaviour of 316L stainless steel produced using selective laser melting.* Fatigue & Fracture of Engineering Materials & Structures.
11. Hautfenne, C., S. Nardone, and E. De Bruycker, *Influence of heat treatments and build orientation on the creep strength of additive manufactured IN718*, in *4th International ECCC Conference*. 2017. p. 26-31.
12. Davies, S.J., et al., *Effects of heat treatment on microstructure and creep properties of a laser powder bed fused nickel superalloy.* Materials & Design, 2018. **159**: p. 39-46.
13. Xu, Z., et al., *Creep behaviour of inconel 718 processed by laser powder bed fusion.* Journal of Materials Processing Technology, 2018. **256**: p. 13-24.
14. Xu, Z., et al., *Effect of post processing on the creep performance of laser powder bed fused Inconel 718.* Additive Manufacturing, 2018. **24**: p. 486-497.
15. Xu, Z., et al., *Defect evolution in laser powder bed fusion additive manufactured components during thermo-mechanical testing.* Dimensional Accuracy and Surface Finish in Additive Manufacturing, 2017: p. 113-115.
16. Frost, H.J. and M.F. Ashby, *Deformation Mechanism Maps*. 1982, Oxford: Pergamont press.
17. Norton, F.H., *The Creep of Steel at High Temperatures*, ed. F.H. Norton. 1929: McGraw-Hill, New York, NY, USA. 90.
18. Webster, G.A., et al., *A Code of Practice for conducting notched bar creep tests and for interpreting the data.* Fatigue & Fracture of Engineering Materials & Structures, 2004. **27**(4): p. 319-342.
19. Hayhurst, D.R., *Creep Rupture under Multiaxial States of Stress.* Journal of Mechanical Physics of Solids, 1972. **20**: p. 381–390.
20. Leckie, F.A., *The constitutive equations of continuum creep damage mechanics.* Philosophical Transactions of the Royal Society of London. Series A, Mathematical and Physical Sciences, 1978. **288**: p. 27-47.
21. Bettinson, A.D., *The Influence of Constraint on the Creep Crack Growth of 316H Stainless Steel*, in *Department of Mechanical Engineering*. 2002, Imperial College London: London.
22. Riley, M., A. Mehmanparest, and C.M. Davies. *Prediction and Validation of Multi-axial Stress State Effects on Creep Failure of Pre-Compressed 316H Stainless Steel*. in *SMiRT-23*. 2015. Manchester, UK.
23. Hares, E.A., et al., *The effect of creep strain rate on damage accumulation in Type 316H austenitic stainless steel.* International Journal of Pressure Vessels and Piping, 2018. **168**: p. 132-141.
24. Othman, A.M., D.R. Hayhurst, and B.F. Dyson, *Skeletal Point Stresses in Circumferentially Notched Tension Bars Undergoing Tertiary Creep Modelled with Physically Based Constitutive Equations.* Proceedings: Mathematical and Physical Sciences, 1993. **441**(1912): p. 343-358.
25. Hyde, T.H., L. Xia, and A.A. Becker, *Prediction of creep failure in aeroengine materials under multi-axial stress states.* International Journal of Mechanical Sciences, 1996. **38**(4): p. 385-403.
26. Kwon, O., C.W. Thomas, and D. Knowles, *Multiaxial stress rupture behaviour and stress-state sensitivity of creep damage distribution in Durehete 1055 and*

2.25Cr1Mo steel. International Journal of Pressure Vessels and Piping, 2004. **81**(6): p. 535-542.
27. Webster, G.A., K.M. Nikbin, and F. Biglari, *Finite element analysis of notched bar skeletal point stresses and dimension changes due to creep.* Fatigue and Fracture of Engineering Materials and Structures, 2004. **27**: p. 297-303.
28. Ejaz, M., *Creep Life Prediction of New and Service Exposed 0.5Cr-0.5Mo-0.25V Steel Pipework*. 2019.
29. Mehmanparast, A., et al., *The influence of pre-compression on the creep deformation and failure behaviour of Type 316H stainless steel.* Engineering Fracture Mechanics, 2013. **110**: p. 52-67.
30. Loveday, M.S., *Considerations on the measurement of creep strain in Bridgman notches.* Materials at High Temperatures, 2004. **21**(3): p. 169-174.
31. Schindelin, J., et al., *Fiji: an open-source platform for biological-image analysis.* Nature Methods, 2012. **9**: p. 676-682.
32. Palli, K., et al., *Real-Time Computer Vision with OpenCV.* Communications of the ACM, 2012. **55**: p. 61-69.
33. Sullivan, C.B. and A. Kaszynski, *PyVista: 3D plotting and mesh analysis through a streamlined interface for the Visualization Toolkit (VTK).* Journal of Open Source Software, 2019. **4**: p. 1450.
34. van der Walt, S., et al., *scikit-image: image processing in Python.* PeerJ, 2014. **2**: p. e453.
35. Liu, L., et al., *Dislocation network in additive manufactured steel breaks strength– ductility trade-off.* Materials Today, 2018.
36. Wang, X., et al., *Microstructure and mechanical properties of stainless steel 316L vertical struts manufactured by laser powder bed fusion process.* Materials Science and Engineering: A, 2018. **736**: p. 27-40.
37. Lei, X., et al., *Notch strengthening or weakening governed by transition of shear failure to normal mode fracture.* Scientific Reports, 2015. **5**: p. 10537.
38. Ronneberg, T., C.M. Davies, and P.A. Hooper, *Revealing relationships between porosity, microstructure and mechanical properties of laser powder bed fusion 316L stainless steel through heat treatment.* Materials & Design, 2020. **189**: p. 108481.
39. Davies, C.M., et al. *Residual stress measurements in a 316L uniaxial samples manufactured by laser powder bed fusion*. in *ASME 2020 Pressure Vessels & Piping Division*. 2020. Minneapolis, Minnesota, USA: ASME.
40. Ainsworth, R.A., *R5 procedures for assessing structural integrity of components under creep and creep–fatigue conditions.* International Materials Reviews, 2006. **51**(2): p. 107-126.